Science Advances
AAAS

advances.sciencemag.org/cgi/content/full/7/21/eabe2265/DC1

Supplementary Materials for

Table-top extreme ultraviolet second harmonic generation

Tobias Helk*, Emma Berger, Sasawat Jamnuch, Lars Hoffmann, Adeline Kabacinski, Julien Gautier, Fabien Tissandier, Jean-Philipe Goddet, Hung-Tzu Chang, Juwon Oh, C. Das Pemmaraju, Tod A. Pascal, Stephane Sebban, Christian Spielmann*, Michael Zuerch*

*Corresponding author. Email: tobias.helk@uni-jena.de (T.H.); christian.spielmann@uni-jena.de (C.S.); mwz@berkeley.edu (M.Z.)

Published 19 May 2021, *Sci. Adv.* **7**, eabe2265 (2021)
DOI: 10.1126/sciadv.abe2265

This PDF file includes:

Processing Experimental Data

Figure S1a depicts a logarithmic image of 146 accumulated single shots of a binned (512 x 512 pixel) camera image. A non-trivial background that increases vertically is observed, which is particularly strong above pixel 40 on the angular axis. Additionally, diffraction spots above the 0^{th} and $\pm 1^{st}$ order peaks along the vertical axis were observed in the raw images. Both of these effects were challenging to remove during the experiment, since a background correction without the sample in the beam path would have been misleading due to the intensity jitter of the SXRL. A post-processing algorithm was implemented to correct for the background that involved manually selecting a sufficient amount of *n* pixels on the image corresponding to the background, fitting a two-variable polynomial of power *n* to the selected pixels, and subtracting the result from each image. A logarithmic image of 248 accumulated and background-corrected single shots of an un-binned camera image (1024 x 1024 pixels) is shown in Figure S1b, with red boxes indicating the regions of analysis. The $\pm 1^{st}$ order peaks are displayed to the left and right of the central peak. The larger peaks on the far right and left correspond to the incident fundamental beam, whereas the smaller peaks second from the left and right correspond to the SHG peaks. A CCD image of the spectrum with no sample present is shown in Fig. S2. Apparent is the lack of SHG signal in between the +/- 1^{st} orders of the fundamental signal, thus confirming that what is deemed SHG is

not an artifact of the instrumentation. Accumulating the 248 raw images was necessary to visualize the SHG peak, as this peak was not apparent in single shot images (Figure S3a – raw image, Figure S3b – background corrected). We note the logarithmic scales of Figs. S1-S3.

To extract the $\chi^{(2)}$ response according to equation (1) in the main text, the spectra were sorted into bins based on the number of photon counts within the areas corresponding to the $\pm1^{st}$ order of the fundamental. Within each bin, the spectra were accumulated and normalized, and the photon counts within areas corresponding to the $\pm1^{st}$ order of the SHG peaks were obtained. The error of the fundamental and SHG yield was calculated assuming Gaussian distribution within each bin and determining the one σ width. For the binned data set, the SHG intensity is on the order of the un-binned data, but with a less intensive fundamental beam. This can be explained by the numerical background correction, since binning increases the yield for each pixel. The simulated background is therefore also higher and reduces the input yield of the fundamental, which makes it harder to compare the both data sets. The square of the pulse energies obtained for the fundamental and that of the SHG peaks were plotted with respect to each other. A linear equation was fit to the data with R^2=0.87. The dependence of the SHG-yield is offset corrected with the y-intercept from the fit function to ensure that zero input intensity of the fundamental corresponds to zero SHG output. A negative yield in this graphs would be caused by this offset subtraction.

The conversion of photon counts on the CCD to on-target pulse energy was performed by measuring the shot-to-shot statistics of the SXRL with a footprint camera in place of the experimental setup and correlating the fluctuations with those observed on the CCD camera. For measuring the pulse energy with the footprint camera, two 0.45 μm thick Al filters (transmission ≈ 2%) and a reflective mirror with an angle of incidence of 45° (reflectivity ≈ 30%) were used to attenuate and steer the SXRL beam onto the camera (quantum efficiency at 37.8 eV ≈ 70%). The beam characterization camera setup was then replaced with one 0.15 μm thick Al filter (transmission ≈ 50%) and an Au ellipsoidal mirror (reflectivity ≈ 70%) and the remainder of the experimental setup as seen in Figure 1a. From this, the average energy of the SXRL was determined to be 111 ± 23 nJ. The pulse energies of the SHG were determined by considering the different optical losses from the beam path taken by the SHG photons from sample to CCD camera (Table S1).

First-Principles Simulation of Linear and Nonlinear Susceptibility

We first assessed the frequency-dependent linear optical response and nonlinear second harmonic susceptibility $\chi^{(2)}$ of the Ti surface by means of density functional perturbation theory (DFPT) calculations using the *exciting*[29] all-electron software package. Structures representing the hexagonal close packed (hcp) Ti bulk and an asymmetric slab were used to simulate the bulk and surface second harmonic response respectively. The Ti surface was modeled as a slab supercell of 6 hcp Ti layers on top a monolayer of Zn with dimensions a = 2.93 Å and c = 27.94 Å along with over 14 Å of vacuum normal to the slab. The Zn monolayer is employed to nominally break inversion symmetry. Here, the formalism by Sharma[28] implemented within *exciting* was used to determine the second-order response. A total of 250 empty states were included in the ground state calculation to account for the excited states, which was deemed enough to increase the number of energy eigenvalues to extend above $2\hbar\omega$, while still being computationally feasible. The Brillouin zone was sampled with a 40x40x1 Γ-point centered k-point grid. A rigid shift of 3.2 eV was necessary to align the DFT linear response to the experimental spectral features.

Real-Time TDDFT Simulation of Linear and Nonlinear Response

The material response of a monochromatic laser field incident on a Ti foil was simulated with real-time velocity gauge[41,42] TDDFT using a linear combination of localized atomic orbitals implemented within SIESTA.[31,43] The linear response of Ti was calculated first as a benchmark for calibrating the laser field energy.[44] Here, we employed a semi-core norm-conserving pseudopotential including Ti 3s and 3p states in the valence band to include the response at the desired Ti-M edge. An 8 layer Ti slab geometry is employed to model the surface. The symmetry of the system was artificially broken by excluding from the bottom 4 layers Ti semi-core 3s and 3p electrons from the valence electron self-consistent field and instead placing them in the core region. Thus Ti M-edge semi-core SHG response is expected to arise from only the top 4 layers of the slab. The Brillouin zone of the slab was sampled with a Γ-centered 20x20x1 *k*-point grid. Exchange-correlation effects within TDDFT were simulated at the level of the Perdew-Zunger local density approximation (LDA-PZ).[45] We employed a basis set of double-ζ quality consisting of {3s(ζ), 3p(ζ), 4s(2ζ), 3d(2ζ), 4p(ζ)} orbitals for a total of 19 atomic orbitals per Ti atom. The real space mesh cutoff was set to 400 Ry. A timestep of 0.04 a.u. (1.935 as) was used to propagate the system.

The current response *J(t)* of bulk Ti induced by a weak impulse electric field of 0.001 a.u. along x- and z-axes at time zero is shown in Fig. S4. Due to the symmetry of bulk Ti, the material response in the x- and y-directions responded identically to the incident field, whereas a different current response was observed along the z-axis. The frequency-dependent dielectric response function $\varepsilon(\omega)$ was then obtained from Fourier transformation of *J(t)*. Here, a maximum in the linear response at 41.6 eV was identified. This was used as the external energy of the laser for simulating the nonlinear light-matter interaction.

To verify that the linear response near 41.6 eV originated from the 3p electrons, we performed a linear response simulation using the same parameters with and without the inclusion of Ti 3p electrons in the valence electron SCF loop. Here, the main feature at 42 eV and the subsidiary feature at 37 eV are suppressed by nearly 66% and 75%, respectively (Fig. S5). Thus, excitations near 37 eV in the linear regime are confirmed to primarily involve Ti 3p to conduction band transitions.

Next, we investigated the interaction of the Ti slab with a monochromatic laser of field of varying intensity ranging from $1x10^{10}$ to $1x10^{13}$ W/cm^2. Under our experimental conditions, we expected an SHG response only at the surface of the Ti as the centrosymmetric bulk extends effectively to infinity. Due to the finite length of the slab in simulations, special care needed to be taken to ensure the SHG response was not predicted from both the front and rear ends of the slab that would cancel each other out and attenuate the SHG signal. Practically, only one Ti surface was made SHG-active by modeling the top half of the supercell with a semi-core electron basis set and the bottom half with a valence pseudopotential that excluded Ti 3s and 3p semi-core states. Further details on this approach can be found in the supplementary information of [17]. Due to the extended nature of highly excited electronic states, ghost atoms were added to the top and bottom of the slab to improve the quality of the nonlinear response. These ghost atoms do not impact the position of spectral peaks and were added to account for potential transitions to states in the continuum that would otherwise be absent in our localized orbital basis set approach. The light-matter interaction was then simulated with a 41.6 eV, 5 fs driving pulse with a sine-squared envelope oriented along z-axis perpendicular to Ti slab supercell. Though 5 fs is significantly shorter than the experimental pulse duration, it is sufficiently long to resonantly probe Ti M-edge excitations. This chosen energy of 41.6 eV corresponds to the maximum in the linear spectral

response from the TDDFT approach. The slab model was propagated in time with different driving laser fields in the 10^{10}-10^{13} W/cm^2 intensity range.

In Fig. S6, we plot the z-component of the time profile of the laser field and the induced current response of the Ti slab. The corresponding Fourier-transformed current *J(ω)* (Fig. S7) demonstrates that the second harmonic response at *2ω* is stronger with stronger laser intensity. The generalized nonlinear susceptibilities can be given by the Taylor-expansion in equation (1) in the main text. This equation is valid in the nonlinear regime and it shows the response at *2ω* scales with the square of the field strength. As shown in the log-log plot in Fig S8 we find that *J(2ω)* exhibits a nearly quadratic dependence with respect to the applied field strength with an R^2 value to the linear fit with slope 1.873 +/- 0.043 of 0.996.

Figures and Tables

Table S1: Parameters used for determining the on-target intensity of the SXRL beam	
Quantum Efficiency of CCD (fundamental)	0.68
Quantum Efficiency of CCD (SHG)	0.82
Grating Efficiency (fundamental, SHG)	0.1
Fraction of beam reflected off toroidal mirror (fundamental)	0.88
Fraction of beam reflected off toroidal mirror (SHG)	0.86
Fraction of beam transmitted through Ti foil (fundamental)	0.019
Fraction of beam transmitted through Ti foil (SHG)	0.48

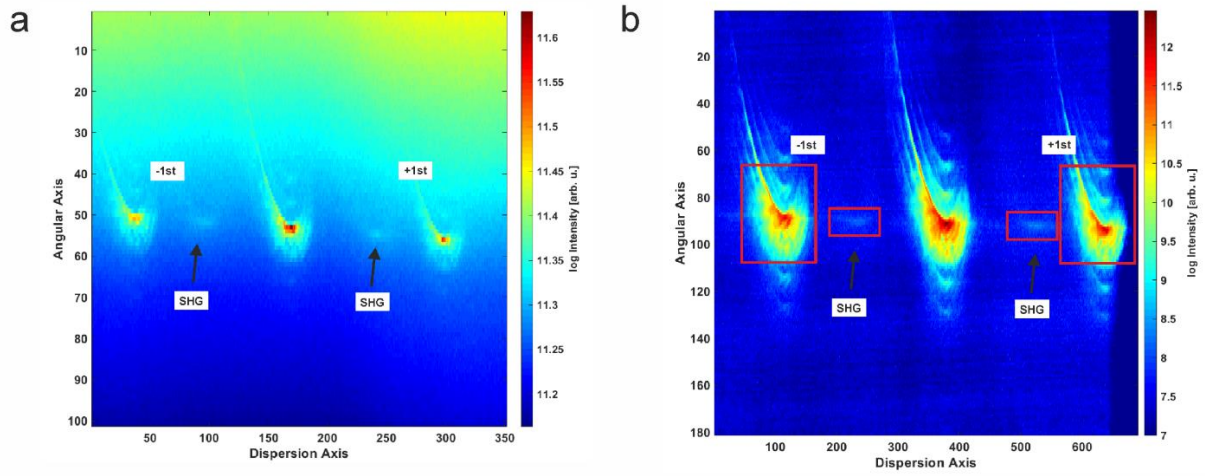

Fig. S1: Raw accumulated and background corrected spectra. a) Logarithmic image of 146 accumulated single shots of a binned camera (512 x 512 pixel). A SHG signal is in between zeroth order and ±1st order visible. b) Logarithmic image of 248 accumulated and background corrected single shots of an unbinned camera (1024 x 1024 pixel). Red boxes indicate the area for the analysis of the fundamental and SHG yield of the single spectra.

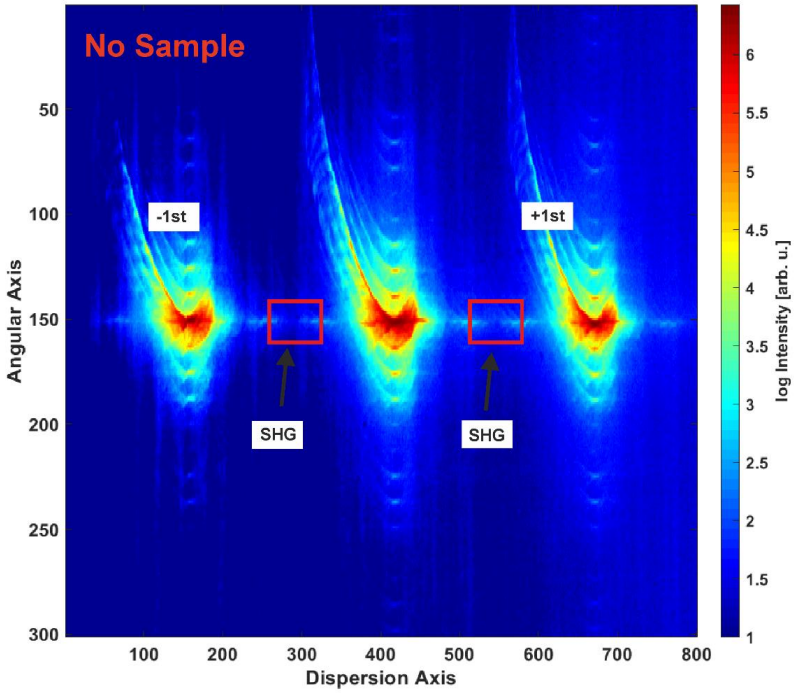

Fig. S2: CCD image of signal with no sample present with 10 shots averaged together. No SHG signal can be seen in the +/- 1st order of where the SHG should be as in Fig. S1. Horizontal streaks appearing on the periphery of the peaks are a result of "ghosting", a well-known phenomenon that can occur with transmission gratings that are imperfectly ruled.

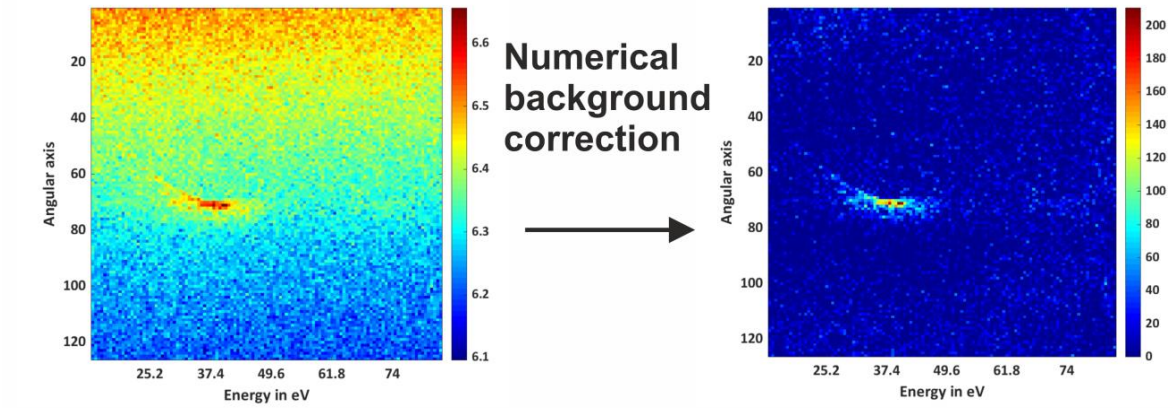

Fig. S3: Impact of background correction. On the left, single shot spectra with noisy background in a logarithmic representation. Applying the numerical background correction, described above, leads to spectra as can be seen on the right. A SHG signal is not clearly visible.

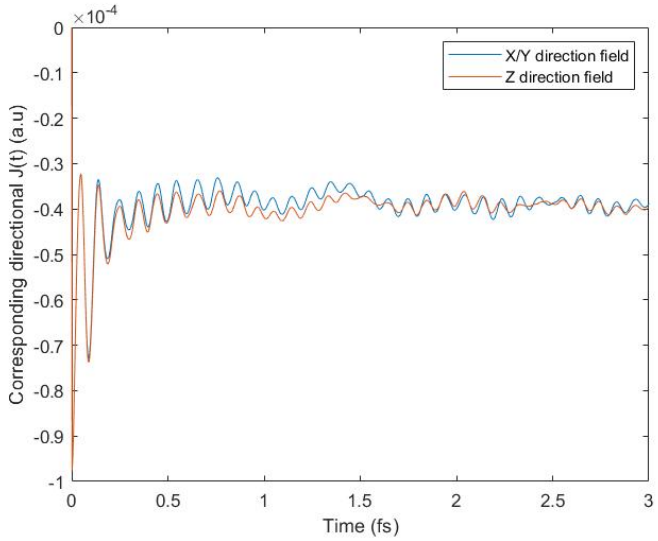

Fig. S4: Current response of bulk titanium to a directional impulse perturbation comparison between x/y and z direction.

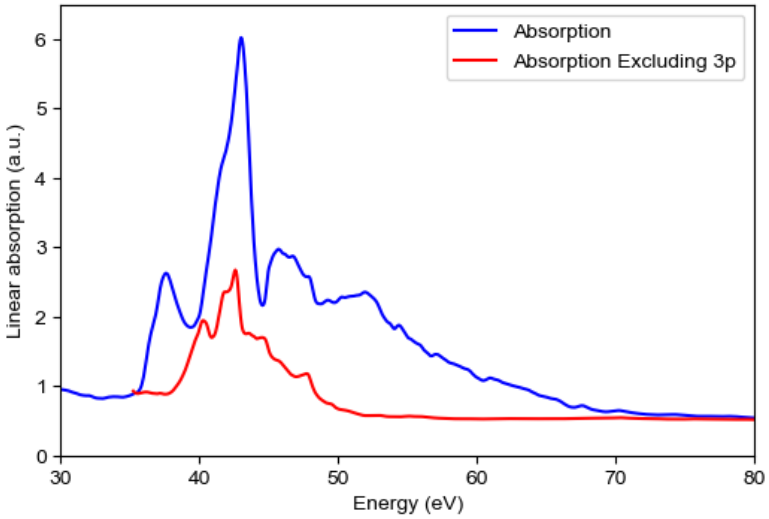

Fig. S5: Linear absorption spectrum with (blue) and without (red) the inclusion of Ti 3p electrons.

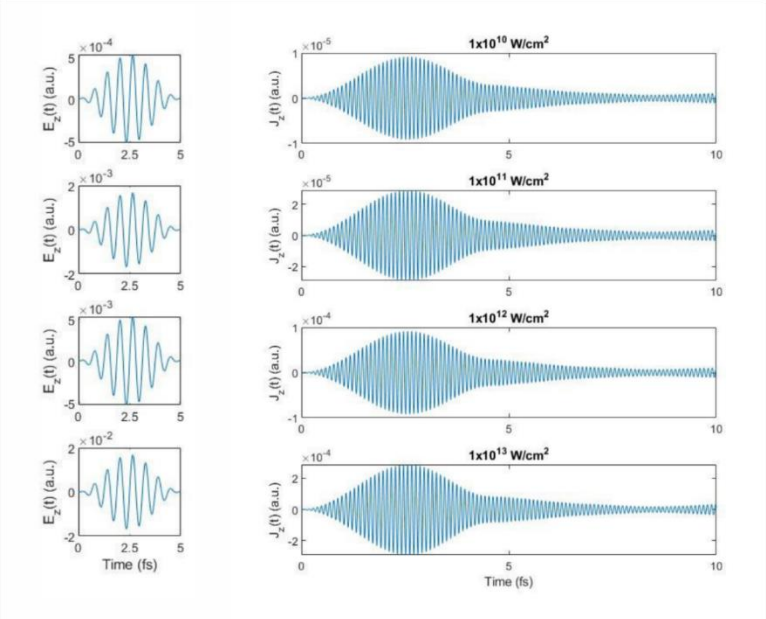

Fig. S6: Interaction of laser pulse with titanium slab (left) Magnitude and time profile of applied laser pulse with intensities ranging from 10^{10}-10^{13} W/cm^2 (right) z-component of time dependent induced current response.

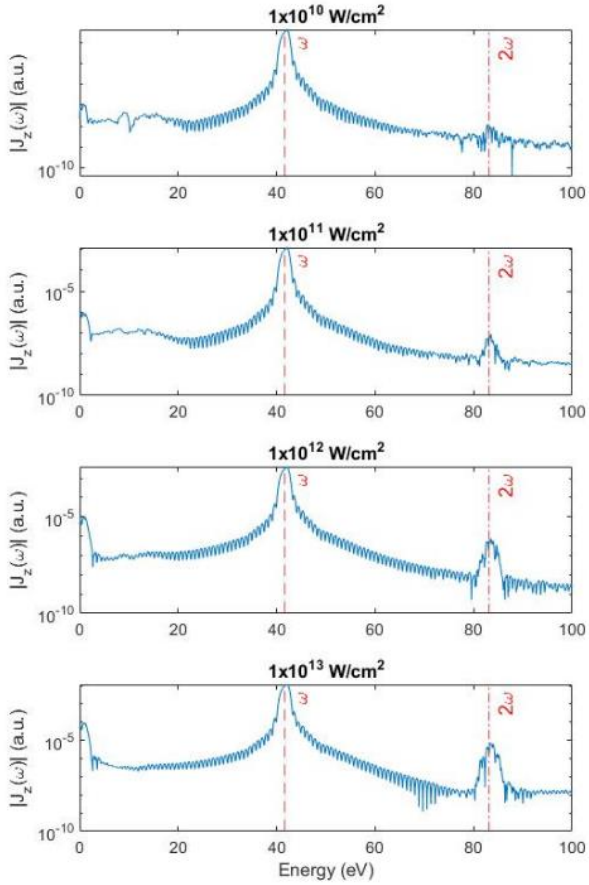

Fig. S7: Frequency domain of z-component current function.

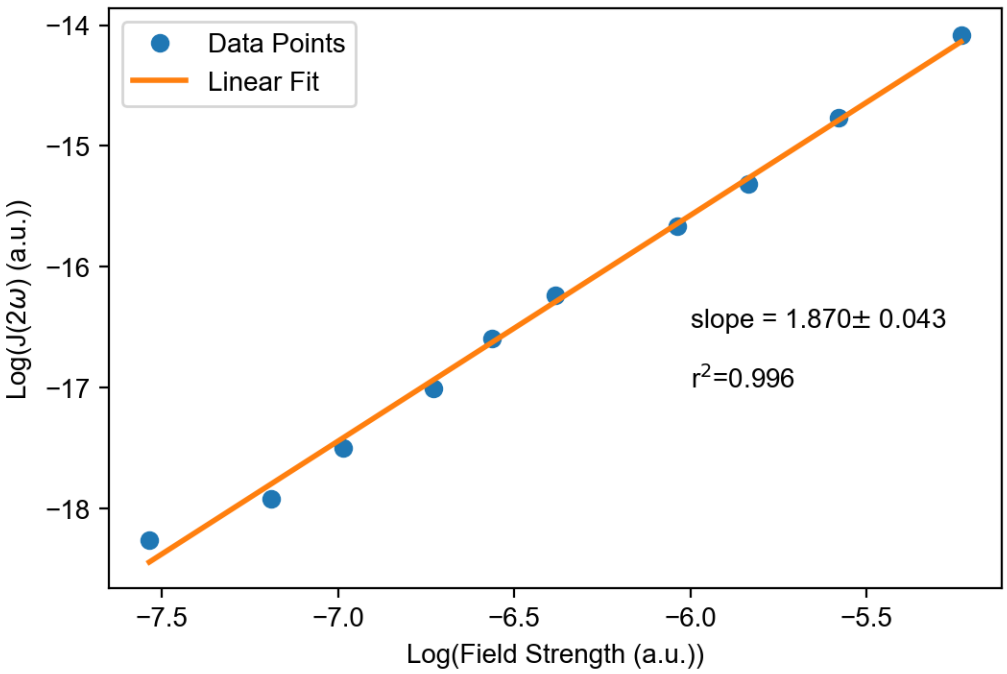

Fig. S8: A log-log plot of the current response at the second harmonic versus field strength exhibits nearly quadratic behavior with a linear best fit slope of 1.870 +/- 0.043, thus confirming that the response at 2ω is indeed second order.

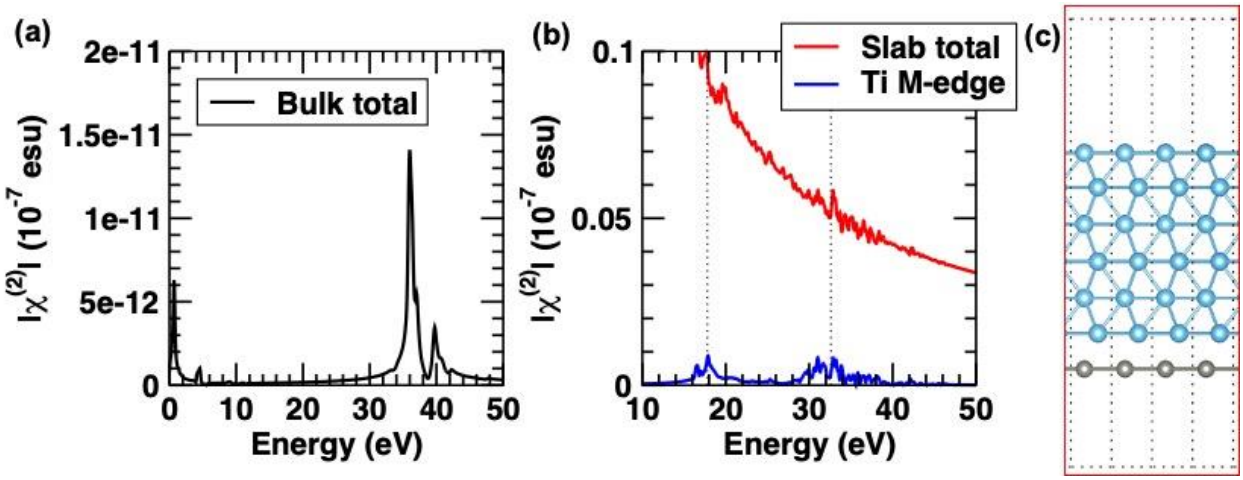

Fig. S9: (a,b) The absolute value of the second order nonlinear susceptibility $\chi^{(2)}$ is shown for bulk titanium and an asymmetric slab model comprised of 6 layers of Ti on a Zn monolayer. An asymmetric slab (shown in panel **(c)**) is needed in the simulation to nominally break inversion symmetry. It is seen that the bulk $\chi^{(2)}$ (a) is 9 orders of magnitude smaller than that of the model Ti surface (b). Also shown separately in (b) is the Ti M-edge resonant contribution to $\chi^{(2)}$ which accounts for roughly 20% of the susceptibility.

REFERENCES AND NOTES

1. E. T. J. Nibbering, D. A. Wiersma, K. Duppen, Ultrafast nonlinear spectroscopy with chirped optical pulses. *Phys. Rev. Lett.* **68**, 514–517 (1992).

2. K. Tanaka, H. Hirori, M. Nagai, THz nonlinear spectroscopy of solids. *IEEE Trans. Terahertz Sci. Technol.* **1**, 301–312 (2011).

3. K. Tamasaku, E. Shigemasa, Y. Inubushi, I. Inoue, T. Osaka, T. Katayama, M. Yabashi, A. Koide, T. Yokoyama, T. Ishikawa, Nonlinear spectroscopy with x-ray two-photon absorption in metallic copper. *Phys. Rev. Lett.* **121**, 083901 (2018).

4. R. W. Boyd, *Nonlinear Optics (3rd Edition)* (Academic Press, 2008).

5. B. E. A. Saleh, M. C. Teich, *Fundamentals of Photonics* (John Wiley & Sons Inc., 1991).

6. P. B. Petersen, R. J. Saykally, On the nature of ions at the liquid water surface. *Annu. Rev. Phys. Chem.* **57**, 333–364 (2006).

7. Y. R. Shen, Surface properties probed by second-harmonic and sum-frequency generation. *Nature* **337**, 519–525 (1989).

8. K. B. Eisenthal, Liquid interfaces probed by second-harmonic and sum-frequency spectroscopy. *Chem. Rev.* **96**, 1343–1360 (1996).

9. Y. R. Shen, Optical second harmonic generation at interfaces. *Annu. Rev. Phys. Chem.* **40**, 327–350 (1989).

10. D. Hsieh, J. W. McIver, D. H. Torchinsky, D. R. Gardner, Y. S. Lee, N. Gedik, Nonlinear optical probe of tunable surface electrons on a topological insulator. *Phys. Rev. Lett.* **106**, 057401 (2011).

11. M. Dantus, Coherent nonlinear spectroscopy: From femtosecond dynamics to control. *Annu. Rev. Phys. Chem.* **52**, 639–679 (2001).

12. T. Yagasaki, S. Saito, Fluctuations and relaxation dynamics of liquid water revealed by linear and nonlinear spectroscopy. *Annu. Rev. Phys. Chem.* **64**, 55–75 (2013).

13. P. M. Kraus, M. Zürch, S. K. Cushing, D. M. Neumark, S. R. Leone, The ultrafast x-ray spectroscopic revolution in chemical dynamics. *Nat. Rev. Chem.* **2**, 82–94 (2018).

14. S. Shwartz, M. Fuchs, J. B. Hastings, Y. Inubushi, T. Ishikawa, T. Katayama, D. A. Reis, T. Sato, K. Tono, M. Yabashi, S. Yudovich, S. E. Harris, X-ray second harmonic generation. *Phys. Rev. Lett.* **112**, 163901 (2014).

15. S. Yamamoto, T. Omi, H. Akai, Y. Kubota, Y. Takahashi, Y. Suzuki, Y. Hirata, K. Yamamoto, R. Yukawa, K. Horiba, H. Yumoto, T. Koyama, H. Ohashi, S. Owada, K. Tono, M. Yabashi, E. Shigemasa, S. Yamamoto, M. Kotsugi, H. Wadati, H. Kumigashira, T. Arima, S. Shin, I. Matsuda, Element selectivity in second-harmonic generation of $GaFeO_3$ by a soft-x-ray free-electron laser. *Phys. Rev. Lett.* **120**, 223902 (2018).

16. E. Berger, S. Jamnuch, C. Uzundal, C. Woodahl, H. Padmanabhan, A. Amado, P. Manset, Y. Hirata, I. Matsuda, V. Gopalan, Y. Kubota, S. Owada, K. Tono, M. Yabashi, Y. Shi, C. Schwartz, W. Drisdell, J. Freeland, T. Pascal, M. Zuerch, Direct observation of symmetry-breaking in a 'ferroelectric' polar metal. arXiv:2010.03134 (2020).

17. R. K. Lam, S. L. Raj, T. A. Pascal, C. D. Pemmaraju, L. Foglia, A. Simoncig, N. Fabris, P. Miotti, C. J. Hull, A. M. Rizzuto, J. W. Smith, R. Mincigrucci, C. Masciovecchio, A. Gessini, E. Allaria, G. De Ninno, B. Diviacco, E. Roussel, S. Spampinati, G. Penco, S. Di Mitri, M. Trovò, M. Danailov, S. T. Christensen, D. Sokaras, T.-C. Weng, M. Coreno, L. Poletto, W. S. Drisdell, D. Prendergast, L. Giannessi, E. Principi, D. Nordlund, R. J. Saykally, C. P. Schwartz, Soft x-ray second harmonic generation as an interfacial probe. *Phys. Rev. Lett.* **120**, 023901 (2018).

18. C. P. Schwartz, S. L. Raj, S. Jamnuch, C. J. Hull, P. Miotti, R. K. Lam, D. Nordlund, C. B. Uzundal, C. D. Pemmaraju, R. Mincigrucci, L. Foglia, A. Simoncig, M. Coreno, C. Masciovecchio, L. Giannessi, L. Poletto, E. Principi, M. Zuerch, T. A. Pascal, W. S. Drisdell, R. J. Saykally, Ångström-resolved interfacial structure in organic-inorganic junctions. arXiv:2005.01905 (2020).

19. K. Midorikawa, Y. Nabekawa, A. Suda, XUV multiphoton processes with intense high-order harmonics. *Prog. Quantum Electron.* **32**, 43–88 (2008).

20. S. Sebban, A. Depresseux, E. Oliva, J. Gautier, F. Tissandier, J. Nejdl, M. Kozlova, G. Maynard, J. P. Goddet, A. Tafzi, A. Lifschitz, H. T. Kim, S. Jacquemot, P. Rousseau, P. Zeitoun, A. Rousse, Toward compact and ultra-intense laser based soft x-ray lasers. *Plasma Phys. Control. Fusion* **60**, 014030 (2018).

21. E. Takahashi, Y. Nabekawa, K. Midorikawa, Generation of 10-μJ coherent extreme-ultraviolet light by use of high-order harmonics. *Opt. Lett.* **27**, 1920–1922 (2002).

22. R. Klas, S. Demmler, M. Tschernajew, S. Hädrich, Y. Shamir, A. Tünnermann, J. Rothhardt, J. Limpert, Table-top milliwatt-class extreme ultraviolet high harmonic light source. *Optica* **3**, 1167–1170 (2016).

23. T. Helk, M. Zürch, C. Spielmann, Perspective: Towards single shot time-resolved microscopy using short wavelength table-top light sources. *Struct. Dyn.* **6**, 010902 (2019).

24. A. Depresseux, E. Oliva, J. Gautier, F. Tissandier, J. Nejdl, M. Kozlova, G. Maynard, J. P. Goddet, A. Tafzi, A. Lifschitz, H. T. Kim, S. Jacquemot, V. Malka, K. Ta Phuoc, C. Thaury, P. Rousseau, G. Iaquaniello, T. Lefrou, A. Flacco, B. Vodungbo, G. Lambert, A. Rousse, P. Zeitoun, S. Sebban, Table-top femtosecond soft x-ray laser by collisional ionization gating. *Nat. Photonics* **9**, 817–821 (2015).

25. B. L. Henke, E. M. Gullikson, J. C. Davis, X-ray interactions: Photoabsorption, scattering, transmission, and reflection at E = 50-30,000 eV, Z = 1-92. *At. Data Nucl. Data Tables* **54**, 181–342 (1993).

26. M. Fuchs, R. Weingartner, A. Popp, Z. Major, S. Becker, J. Osterhoff, I. Cortrie, B. Zeitler, R. Hörlein, G. D. Tsakiris, U. Schramm, T. P. Rowlands-Rees, S. M. Hooker, D. Habs, F. Krausz, S. Karsch, F. Grüner, Laser-driven soft-x-ray undulator source. *Nat. Phys.* **5**, 826–829 (2009).

27. P. Hohenberg, W. Kohn, Inhomogeneous electron gas. *Phys. Rev.* **136**, B864–B871 (1964).

28. S. Sharma, C. Ambrosch-Draxl, Second-harmonic optical response from first principles. *Phys. Scr.* **T109**, 128–134 (2004).

29. A. Gulans, S. Kontur, C. Meisenbichler, D. Nabok, P. Pavone, S. Rigamonti, S. Sagmeister, U. Werner, C. Draxl, Exciting: A full-potential all-electron package implementing density-functional theory and many-body perturbation theory. *J. Phys. Condens. Matter* **26**, 363202 (2014).

30. S. Sagmeister, C. Ambrosch-Draxel, Time-dependent density functional theory versus Bethe-Salpeter equation: An all-electron study. *Phys. Chem. Chem. Phys.* **11**, 4451–4457 (2009).

31. J. M. Soler, E. Artacho, J. D. Gale, A. García, J. Junquera, P. Ordejón, D. Sánchez-Portal, The SIESTA method for ab initio order-*N* materials simulation. *J. Phys. Condens. Matter* **14**, 2745–2779 (2002).

32. K. Yamamoto, Y. Kubota, M. Suzuki, Y. Hirata, K. Carva, M. Berritta, K. Takubo, Y. Uemura, R. Fukaya, K. Tanaka, W. Nishimura, T. Ohkochi, T. Katayama, T. Togashi, K. Tamasaku, M. Yabashi, Y. Tanaka, T. Seki, K. Takanashi, P. M. Oppeneer, H. Wadati, Ultrafast demagnetization of Pt magnetic moment in $L1_0$-FePt probed by magnetic circular dichroism at a hard x-ray free electron laser. *New J. Phys.* **21**, 123010 (2019).

33. I. Makos, I. Orfanos, A. Nayak, J. Peschel, B. Major, I. Liontos, E. Skantzakis, N. Papadakis, C. Kalpouzos, M. Dumergue, S. Kühn, K. Varju, P. Johnsson, A. L'Huillier, P. Tzallas, D. Charalambidis, A 10-gigawatt attosecond source for non-linear XUV optics and XUV-pump-XUV-probe studies. *Sci. Rep.* **10**, 3759 (2020).

34. O. Jahn, V. E. Leshchenko, P. Tzallas, A. Kessel, M. Krüger, A. Münzer, S. A. Trushin, G. D. Tsakiris, S. Kahaly, D. Kormin, L. Veisz, V. Pervak, F. Krausz, Z. Major, S. Karsch, Towards intense isolated attosecond pulses from relativistic surface high harmonics. *Optica* **6**, 280–287 (2019).

35. P. Tzallas, D. Charalambidis, N. A. Papadogiannis, K. Witte, G. D. Tsakiris, Direct observation of attosecond light bunching. *Nature* **426**, 267–271 (2003).

36. E. J. Takahashi, P. Lan, O. D. Mücke, Y. Nabekawa, K. Midorikawa, Attosecond nonlinear optics using gigawatt-scale isolated attosecond pulses. *Nat. Commun.* **4**, 2691 (2013).

37. F. Ferrari, F. Calegari, M. Lucchini, C. Vozzi, S. Stagira, G. Sansone, M. Nisoli, High-energy isolated attosecond pulses generated by above-saturation few-cycle fields. *Nat. Photonics* **4**, 875–879 (2010).

38. B. Manschwetus, L. Rading, F. Campi, S. Maclot, H. Coudert-Alteirac, J. Lahl, H. Wikmark, P. Rudawski, C. M. Heyl, B. Farkas, T. Mohamed, A. L'Huillier, P. Johnsson, Two-photon double ionization of neon using an intense attosecond pulse train. *Phys. Rev. A* **93**, 061402(R) (2016).

39. E. Oliva, A. Depresseux, M. Cotelo, A. Lifschitz, F. Tissandier, J. Gautier, G. Maynard, P. Velarde, S. Sebban, Hydrodynamic evolution of plasma waveguides for soft-x-ray amplifiers. *Phys. Rev. E* **97**, 023203 (2018).

40. A. Jain, S. P. Ong, G. Hautier, W. Chen, W. D. Richards, S. Dacek, S. Cholia, D. Gunter, D. Skinner, G. Ceder, K. A. Persson, Commentary: The Materials Project: A materials genome approach to accelerating materials innovation. *APL Mater.* **1**, 011002 (2013).

41. K. Yabana, G. F. Bertsch, Time-dependent local-density approximation in real time. *Phys. Rev. B Condens. Matter Mater. Phys.* **54**, 4484–4487 (1996).

42. G. F. Bertsch, J.-I. Iwata, A. Rubio, K. Yabana, Real-space, real-time method for the dielectric function. *Phys. Rev. B Condens. Matter Mater. Phys.* **62**, 7998–8002 (2000).

43. C. D. Pemmaraju, F. D. Vila, J. J. Kas, S. A. Sato, J. J. Rehr, K. Yabana, D. Prendergast, Velocity-gauge real-time TDDFT within a numerical atomic orbital basis set. *Comput. Phys. Commun.* **226**, 30–38 (2018).

44. Y. Takimoto, F. D. Vila, J. J. Rehr, Real-time time-dependent density functional theory approach for frequency-dependent nonlinear optical response in photonic molecules. *J. Chem. Phys.* **127**, 154114 (2007).

45. J. P. Perdew, A. Zunger, Self-interaction correction to density-functional approximations for many-electron systems. *Phys. Rev. B* **23**, 5048–5079 (1981).